

Patchwork: Concentric Zone-based Region-wise Ground Segmentation with Ground Likelihood Estimation Using a 3D LiDAR Sensor

Hyungtae Lim¹, *Student Member, IEEE*, Minho Oh¹, Hyun Myung¹, *Senior Member, IEEE*

Abstract—Ground segmentation is crucial for terrestrial mobile platforms to perform navigation or neighboring object recognition. Unfortunately, the ground is not flat, as it features steep slopes; bumpy roads; or objects, such as curbs, flower beds, and so forth. To tackle the problem, this paper presents a novel ground segmentation method called *Patchwork*, which is robust for addressing the under-segmentation problem and operates at more than 40 Hz. In this paper, a point cloud is encoded into a Concentric Zone Model–based representation to assign an appropriate density of cloud points among bins in a way that is not computationally complex. This is followed by Region-wise Ground Plane Fitting, which is performed to estimate the partial ground for each bin. Finally, Ground Likelihood Estimation is introduced to dramatically reduce false positives. As experimentally verified on SemanticKITTI and rough terrain datasets, our proposed method yields promising performance compared with the state-of-the-art methods, showing faster speed compared with existing plane fitting–based methods. Code is available: <https://github.com/LimHyungTae/patchwork>

Index Terms—Range Sensing; Mapping; Field Robots; Ground Segmentation

I. INTRODUCTION

IN recent years, there has been an increased demand to perceive surroundings for mobile platforms, such as Unmanned Ground Vehicles (UGVs), Unmanned Aerial Vehicles (UAVs), or autonomous cars. To accomplish this, numerous researchers have applied various 3D perception methods [1]–[4]. In particular, a 3D light detection and ranging (LiDAR) sensor has been extensively deployed due to allowing for centimeter-level accuracy and omnidirectional sensing, as well as its ability to measure great distances compared with stereo cameras [1], [5], [6]. Accordingly, a 3D point cloud captured by a LiDAR sensor is utilized for semantic segmentation [7], [8], tracking [9], detection [10], and so forth.

In this paper, we specifically focus on ground segmentation tasks [11], [12]. There are two main purposes of ground segmentation. One is to estimate the movable area [3], [13] for

This work was supported by the Industry Core Technology Development Project, 20005062, Development of Artificial Intelligence Robot Autonomous Navigation Technology for Agile Movement in Crowded Space, funded by the Ministry of Trade, Industry & Energy (MOTIE, Republic of Korea) and by the research project “Development of A.I. based recognition, judgement and control solution for autonomous vehicle corresponding to atypical driving environment,” which is financed from the Ministry of Science and ICT (Republic of Korea) Contract No. 2019-0-00399. The students are supported by the BK21 FOUR from the Ministry of Education (Republic of Korea).

¹Hyungtae Lim, ¹Minho Oh, and ¹Hyun Myung are with the School of Electrical Engineering, KI-AI, KI-R at KAIST (Korea Advanced Institute of Science and Technology), Daejeon, 34141, South Korea. {shapelim, minho.oh, hmyung}@kaist.ac.kr

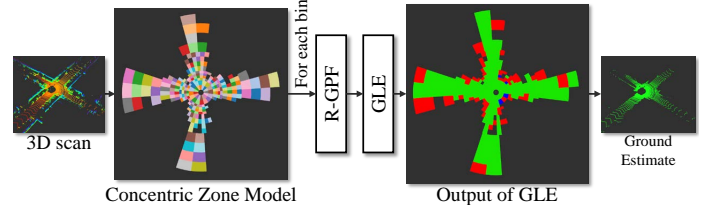


Fig. 1. Overview of our proposed method called *Patchwork*. Patchwork mainly consists of three parts: Concentric Zone Model (CZM)–based polar grid representation, Region-wise Ground Plane Fitting (R-GPF), and Ground Likelihood Estimation (GLE).

successful navigation. The other purpose, on which this paper places more emphasis, is the segmentation of a point cloud to recognize or track moving objects. Terrestrial vehicles or humans inevitably come into contact with the ground [14]; ideally, dynamic objects can be recognized in a simple way, such as through Euclidean clustering if the ground is well estimated [8], [15]. Furthermore, because most cloud points belong to the ground, ground segmentation can significantly reduce computational power when one is performing object segmentation or detection in a preprocessing stage [16]. Thus, *ground* in this study refers to not only the road, which is a movable area, but also all regions that moving objects can come into contact with, including sidewalks or lawns.

In this study, as presented in Fig. 1, we propose a novel Concentric Zone Model (CZM)–based region-wise ground segmentation method, called *Patchwork*, which is an extension of Region-wise Ground Plane Fitting (R-GPF) in our previous study [14]. The aim of R-GPF in our previous study was to estimate the ground points for static map building purposes, whereas here, we focus only on ground segmentation on a 3D point cloud. We also conduct detailed experiments on the impact of the bin size, which was not covered in our previous paper.

In summary, the contribution of this paper is threefold:

- To the best of our knowledge, it is the first attempt to analyze the impact of bin size when estimating ground planes in complex urban environments using the SemanticKITTI dataset [1]. Accordingly, an efficient, non-uniform, region-wise representation of a 3D point cloud is proposed, referred to as a CZM–based representation whose bin size is different depending on each zone.
- Also, we leverage Ground Likelihood Estimation (GLE) in terms of *uprightness*, *elevation*, and *flatness* to deter-

mine whether each bin is ground.

- Our proposed method shows promising performance over the state-of-the-art, region-wise fitting-based methods at more than 40 Hz. In particular, Patchwork estimates the ground points with the least recall variance, which shows that our proposed method overcomes the under-segmentation issue in complex urban environments.

II. RELATED WORKS

A. The Difficulties of Ground Segmentation

One may argue that it is a simple task that can be easily estimated by filtering a point cloud based on sensor height or using RANSAC [17] which is a renowned method for estimating a plane. Unfortunately, there are three main issues that impede algorithms from conducting precise ground segmentation: a) there exists a partially steep slope or bumpy road, b) curbs or flower beds make some regions uneven, and c) because all surrounding objects are taken into account as outliers in the ground segmentation tasks, these objects hinder plane fitting. For these reasons, sometimes under-segmentation occurs, in which case points belonging to different objects are merged into the same segment [6], [12].

B. Ground Plane Estimation Methods

To tackle these issues, numerous researchers have studied various approaches. For instance, Douillard *et al.* [4] and Chen *et al.* [18] employed Gaussian process-based methods. On the other hand, Tse *et al.* [19], Byun *et al.* [3], and Rummelhard *et al.* [20] proposed Markov Random Field-based methods. These methods can be used to estimate detailed ground points yet requiring much computational time, so it may not be appropriate to use them as preprocessing algorithms whose speed should be guaranteed at more than 20 Hz.

C. Scan Representation

Meanwhile, grid representation-based methods have been widely utilized to leverage expressibility compared with singular plane model-based methods [4], [9]. In particular, polar grid representation, which treats a point cloud in cylindrical coordinates, is commonly employed these days because it naturally compensates for the geometric characteristics of 3D LiDAR sensors [11], [12], [14], [16], [21]. In practice, Thrun *et al.* [5] presented a grid cell-based binary ground classification method in a probabilistic way to predict the movable area for autonomous driving in the DARPA challenge. These methods are mainly divided into two categories: a) elevation map-based and b) model fitting-based methods. Accordingly, the latter category can be further classified into two main methodologies: a) line fitting-based and b) plane fitting-based methods.

D. Elevation Map-based 2.5D Grid Representation

First, elevation map-based methods are used to distinguish between ground and non-ground points by encoding a 3D point cloud into 2.5D grid representations [5], [9]. Thrun *et al.* [5] utilized relative height and Asvadi *et al.* [9] used average height and its covariance on each grid. These methods have strong advantages over other methods in terms of speed and

computational cost. However, there are some potential risks that sometimes a steep slope region could be considered as a non-ground region because of large z value difference between its supremum and infimum points with respect to Z-axis.

E. Multiple Line Fitting-based Ground Segmentation

Next, Himmelsbach *et al.* [11] and Steinhauser *et al.* [21] introduced 2D line fitting on a uniform polar grid representation to estimate the straight-line equation on each grid. Then, in each grid, it was determined whether points were ground points by comparing between constant thresholds and the estimated parameters, such as the point-to-line distance, gradient, or y-intercept.

F. Multiple Plane Fitting-based Ground Segmentation

Sharing their views of region-wise fitting yet improving robustness, other researchers have conducted region-wise plane fitting-based approaches [8], [12], [14], [16]. For instance, Zermas *et al.* [8] divided a point cloud into three parts along the x-axis of the body frame, which is the forward direction of a vehicle. This method is based on the premise that a slope usually changes along the x-axis; however, this assumption sometimes fails when it comes to a bumpy road or a complex intersection. To resolve the problem, Narksri *et al.* [12] proposed a slope-robust method using consecutive ring patterns in the scan data as well as the concept of the continuity of the region-wise estimated plane along the radial direction. Furthermore, Narksri *et al.* [12] and Cheng *et al.* [16] proposed an adaptive way of setting a grid size depending on the density of the cloud points or the incidence angle.

G. Deep Learning-based Methods

Of course, as the deep learning era has come, Milioto *et al.* [7] proposed RangeNet++ to estimate point-wise labels on a 3D point cloud and Paigwar *et al.* [22] presented GndNet, which estimates ground plane elevation information in a grid-based representation to discern ground points in real time. Unfortunately, these methods usually require high computational resources. In addition, these methods tend to be highly fitted to the environments of train dataset; thus, the performance of those can be potentially degraded when used in quite different environments from the training dataset or different sensor configuration [23].

III. METHODOLOGY OF PATCHWORK

The following paragraphs highlight the problem definition and the reasoning behind each module of Patchwork. Patchwork mainly consists of three parts: CZM, R-GPF, and GLE.

A. Problem Definition

First, we begin by denoting a point cloud at the moment as \mathcal{P} . Then, let $\mathcal{P} = \{\mathbf{p}_1, \mathbf{p}_2, \dots, \mathbf{p}_k, \dots, \mathbf{p}_N\}$ be a set of cloud points that contain N points at the moment acquired by a 3D LiDAR sensor, where each point \mathbf{p}_k consists of $\mathbf{p}_k = \{x_k, y_k, z_k\}$ in the Cartesian coordinates. In this paper, \mathcal{P} is definitely classified into two classes: a set of ground points, G , and its complement, G^c , which satisfy $G \cup G^c = \mathcal{P}$. Note

that G^c denotes non-ground points, including vehicles, walls, street trees, pedestrians, and so forth.

Next, estimated ground points could be defined as \hat{G} . Because the estimation unavoidably contains inherent errors [2], some points that are, in fact, from non-ground objects could be included in \hat{G} , and vice versa. In summary, \hat{G} and \hat{G}^c are expressed as follows:

$$\hat{G} = TP \cup FP \text{ and } \hat{G}^c = FN \cup TN \quad (1)$$

where \hat{G} and \hat{G}^c also satisfy $\hat{G} \cup \hat{G}^c = \mathcal{P}$, and TP, FP, FN, and TN denote sets of *true positives*, *false positives*, *false negatives*, and *true negatives*, respectively. Thus, our goal is to discern \hat{G} and \hat{G}^c from a point cloud \mathcal{P} while estimating as few FPs and FNs as possible.

B. Concentric Zone Model

As mentioned earlier, most multiple plane-based methods are based on the general assumption that the observable world might not be flat. Therefore, ground plane estimation should be conducted region-wise by assuming that small parts, or bins, of the possibly non-flat world and the ground can indeed be flat within the region.

Accordingly, some previous approaches utilized uniform polar grid representation, or S , to divide a point cloud into multiple bins with regular intervals of radial and azimuthal directions, i.e. *rings* and *sectors* [14]. More concretely, let N_r and N_θ be the numbers of rings and sectors, respectively. Then, S is divided into equal-sized bins whose size is L_{\max}/N_r in the radial direction, where L_{\max} denotes the maximum boundary, and $2\pi/N_\theta$ in the azimuthal direction as shown in Fig. 2(a).

Unfortunately, as shown in Fig. 2(c), the experimental evidence, which is measured on whole sequences on the SemanticKITTI dataset [1] to take generalization into account, shows that most ground points are located close to the sensor frame. That is, more than 90% of points belonging to the ground are located within 20 m.

For this reason, S has two limitations. First, as the distance becomes farther away, a point cloud becomes too sparse to find the right ground plane, which we refer to as the *sparsity issue*. Some approaches adaptively adjust the size of a bin to cope with the logarithmic point distribution [11], [12], [16]. However, the bin size increases in a linear or quadratic way, so the sparsity issue is not completely resolved. On the other hand, when the size of the bins located close to the origin is too small to represent a unit space in S , this sometimes leads to the failure of the right normal vector estimation of the ground plane, which we refer to as the *representability issue*.

For addressing these issues, the CZM-based polar grid representation, which is denoted as \mathcal{C} , is proposed to assign the appropriate density among bins in a way that is not computationally complex. Accordingly, \mathcal{P} is divided into multiple zones, each of which is composed of bins of different sizes, as shown in Fig. 2(b). Let $\langle N \rangle = \{1, 2, \dots, N\}$, then our proposed model is defined as follows:

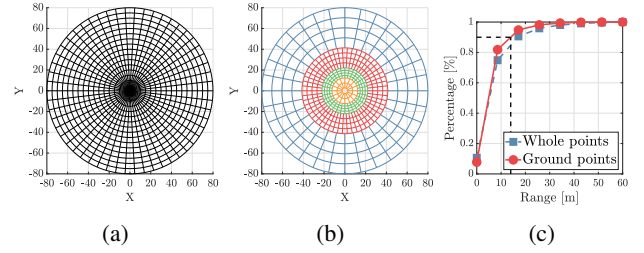


Fig. 2. (a) The uniform polar grid description [11], [14], [21] (b) Our CZM-based polar grid description (c) Cumulative Distribution Function (CDF) of the range, in which more than 90% of ground points are located within 20 m.

$$\mathcal{C} = \bigcup_{m \in \langle N_Z \rangle} Z_m \quad (2)$$

where Z_m denotes the m -th zone of \mathcal{C} and N_Z denotes the number of zones, which is empirically set to four in this paper. Let $Z_m = \{\mathbf{p}_k \in \mathcal{P} \mid L_{\min,m} \leq \rho_k < L_{\max,m}\}$, where $L_{\min,m}$ and $L_{\max,m}$ denote the minimum and the maximum radial boundary of Z_m , respectively; then, Z_m is also divided into $N_{r,m} \times N_{\theta,m}$ bins, where each zone has a different bin size. Accordingly, each bin $\mathcal{S}_{i,j,m}$ is defined as follows:

$$\mathcal{S}_{i,j,m} = \left\{ \mathbf{p}_k \in Z_m \mid \frac{(i-1) \cdot \Delta L_m}{N_{r,m}} \leq \rho_k - L_{\min,m} < \frac{i \cdot \Delta L_m}{N_{r,m}}, \right. \\ \left. \frac{(j-1) \cdot 2\pi}{N_{\theta,m}} - \pi \leq \theta_k < \frac{j \cdot 2\pi}{N_{\theta,m}} - \pi \right\}. \quad (3)$$

where $\rho_k = \sqrt{x_k^2 + y_k^2}$, $\theta_k = \arctan 2(y_k, x_k)$, $\Delta L_m = L_{\max,m} - L_{\min,m}$, and $L_{\max,m} = L_{\min,m+1}$ on $m = 1, 2, 3$. Note that $L_{\max,4} = L_{\max}$ and $L_{\min,1} = L_{\min}$, for which the global minimum boundary L_{\min} is used to consider emptiness over the vicinity of mobile platforms or vehicles. In fact, Z_1 , Z_2 , Z_3 , and Z_4 are called the *central zone*, *quater zone*, *half zone*, and *outer zone*, respectively. Accordingly, $L_{\min,2} = \frac{7 \cdot L_{\min} + L_{\max}}{8}$, $L_{\min,3} = \frac{3 \cdot L_{\min} + L_{\max}}{4}$, and $L_{\min,4} = \frac{L_{\min} + L_{\max}}{2}$.

Note that the sizes of bins in Z_1 and Z_4 are set larger to resolve the sparsity issue and representability issue. Accordingly, \mathcal{C} improves expressibility and thus allows robust estimation of a normal vector compared with the existing uniform representations, thus preventing under-segmentation [11], [14]. Furthermore, it reduces the actual number of bins, for instance, from 3,240 in S to 504 in \mathcal{C} , thus enabling operation at more than 40 Hz (see Section IV.E).

C. Region-wise Ground Plane Fitting

Thereafter, each bin assigns an estimated partial ground via R-GPF; then, the partial ground points are merged later. In this paper, Principal Component Analysis (PCA) is utilized rather than using RANSAC. Of course, RANSAC tends to be less sensitive to outliers compared with PCA [17], [24]. However, using PCA shows much faster speed than using RANSAC and shows acceptable performance [8]; thus, PCA-based estimation is more appropriate as a preprocessing process. Additionally, experiments show that PCA-based methods

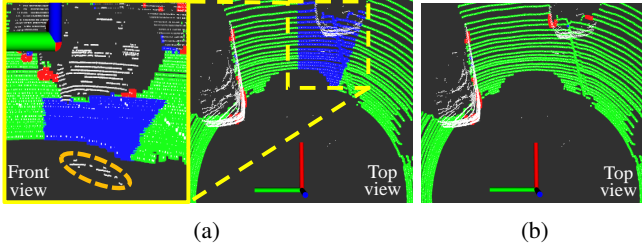


Fig. 3. (a) Before and (b) after the application of adaptive initial seed selection to prevent the effect of erroneous points, which are in dashed lines, on R-GPF for the SemanticKITTI dataset [1] sequence 00 around frame 435. In (a), the mis-measured points, which are inside the dashed circle, are sometimes selected as initial seeds and then cause the failure of region-wise ground plane fitting, which is represented by the blue region. In this paper, the green, blue, and red points denote TPs, FNs, and FPs, respectively. The less blue points are, the better it is (best viewed in color).

are at least two times faster than RANSAC-based methods (see Section IV.E).

Given a bin, let $C \in \mathbb{R}^{3 \times 3}$ be the covariance matrix of cloud points in the unit space; three eigenvalues λ_α and the corresponding three eigenvectors \mathbf{v}_α are calculated as follows:

$$C \mathbf{v}_\alpha = \lambda_\alpha \mathbf{v}_\alpha \quad (4)$$

where $\alpha = 1, 2, 3$, and assume $\lambda_1 \geq \lambda_2 \geq \lambda_3$. Then, the eigenvector that corresponds to the smallest eigenvalue, i.e. \mathbf{v}_3 , is the most likely to represent the normal vector to the ground plane. Therefore, let $\mathbf{n} = \mathbf{v}_3 = [a \ b \ c]^T$; then, the plane coefficient can be calculated as $d = -\mathbf{n}^T \bar{\mathbf{p}}$, where $\bar{\mathbf{p}}$ denotes the mean point of a unit space.

For simplicity, let the n -th bin be S_n over all bins, whose number is equal to $N_C = \sum_{m=1}^{N_Z} N_{r,m} \times N_{\theta,m}$. If the cardinality of S_n is large enough, the lowest-height points are selected to be used as initial seeds. Indeed, the points of each bin with the lowest heights are most likely to belong to the ground surface [8], [11], [12]. Let \bar{z}_{init} be the mean z value of the total N_{seed} number of the selected seed point; then, initial estimated ground points set \hat{G}_n^0 is obtained as follows:

$$\hat{G}_n^0 = \{\mathbf{p}_k \in S_n \mid z(\mathbf{p}_k) < \bar{z}_{\text{init}} + z_{\text{seed}}\} \quad (5)$$

where $z(\cdot)$ returns the z value of a point and z_{seed} denotes the height margin.

Because our method is iterative, let the estimated ground points set on the l -th iteration be \hat{G}_n^l . Then, the normal vector of \hat{G}_n^l , which is denoted as \mathbf{n}_n^l , is obtained through (4) using the points in \hat{G}_n^l . Next, plane coefficient d_n^l is calculated as $d_n^l = -(\mathbf{n}_n^l)^T \bar{\mathbf{p}}_n^l$, where $\bar{\mathbf{p}}_n^l$ denotes the mean point of \hat{G}_n^l . Finally, \hat{G}_n^{l+1} is formulated as follows:

$$\hat{G}_n^{l+1} = \{\mathbf{p}_k \in S_n \mid d_n^l - \hat{d}_k < M_d\} \quad (6)$$

where $\hat{d}_k = -(\mathbf{n}_n^l)^T \mathbf{p}_k$ and M_d denotes the distance margin of the plane. The procedure is repeated multiple times. According to Zermas *et al.* [8], $\hat{G}_n = \hat{G}_n^3$ is empirically the final output on each S_n in this paper.

Note that the main difference between the original R-GPF [14] and ours is that ours involves using adaptive initial seed selection to prevent R-GPF from converging to a local

minimum. Occasionally, erroneous cloud points below the actual ground are acquired due to the multipath problem or reflection of LiDAR signals, as shown in Fig. 3(a) [25]. It is observed that this phenomenon mostly happens in Z_1 because reflection occurs only in areas where the signal is relatively strong. These outliers impede R-GPF from estimating the right ground plane.

To address this issue, we utilize the fact that the z values of ground points only in Z_1 are mainly distributed near $-h_s$, where h_s represents the sensor height. Accordingly, \mathbf{p}_k in S_n which belongs to Z_1 is filtered out if the z_k is lower than $M_h \cdot h_s$ when one is estimating \hat{G}_n^0 , where $M_h < -1$ is the height margin. For an S_n that does not belong to Z_1 , the adaptive threshold decreases as m becomes larger to avoid the improper filtering of points that may come from downhill, which are actually TP.

D. Ground Likelihood Estimation

Consequently, it is necessary to robustly discern whether \hat{G}_n belongs to the actual ground. To this end, GLE is proposed, which is a region-wise probabilistic test for binary classification. In doing so, Patchwork leverages GLE to improve the overall precision, excluding the initial unintended planes consisting of non-ground points.

Let $\mathcal{L}(\theta \mid \mathcal{X})$ be the GLE, where θ denotes all parameters of Patchwork and \mathcal{X} represents a random variable following a continuous probability distribution with density function f . Let us presume that every bin is independent of each other. Then, $\mathcal{L}(\theta \mid \mathcal{X})$ is expressed as

$$\mathcal{L}(\theta \mid \mathcal{X}) = f(\mathcal{X} \mid \theta) = \prod_n f(\mathcal{X}_n \mid \theta_n) \quad (7)$$

where θ_n and \mathcal{X}_n represent parameters and a random variable of each \hat{G}_n , respectively. Note that subscript n denotes that the parameters are from \hat{G}_n .

Based on our prior knowledge, how likely each \hat{G}_n is to be ground points is defined in terms of *uprightness*, *elevation*, and *flatness*, which are represented as $\phi(\cdot)$, $\psi(\cdot)$, and $\varphi(\cdot)$, respectively, as follows:

$$f(\mathcal{X}_n \mid \theta_n) \equiv \phi(\mathbf{v}_{3,n}) \cdot \psi(\bar{z}_n, r_n) \cdot \varphi(\psi(\bar{z}_n, r_n), \sigma_n) \quad (8)$$

where \bar{z}_n , r_n , and σ_n denote the mean z value, the distance between the origin and the centroid of a S_n , and the surface variable, where $\sigma_n = \frac{\lambda_{3,n}}{\lambda_{1,n} + \lambda_{2,n} + \lambda_{3,n}}$ [26], respectively.

Uprightness Indeed, if \hat{G}_n belongs to the actual ground (i.e. most of the points are in TP), it is observed that $\mathbf{v}_{3,n}$ is likely to be orthogonal to the ground with which terrestrial vehicles are in contact. In other words, $\mathbf{v}_{3,n}$ tends to be upright against the X-Y plane of the sensor frame. Therefore, uprightness indicator function is proposed to leverage the geometric characteristics as

$$\phi(\mathbf{v}_{3,n}) = \begin{cases} 1, & \text{if } \frac{\mathbf{v}_{3,n} \cdot \mathbf{z}}{\|\mathbf{v}_{3,n}\| \|\mathbf{z}\|} > \cos(\frac{\pi}{2} - \theta_\tau) \\ 0, & \text{otherwise} \end{cases} \quad (9)$$

where $\mathbf{z} = [0 \ 0 \ 1]$ and θ_τ is the uprightness margin, which denotes the angle between $\mathbf{v}_{3,n}$ and the X-Y plane. That is, the larger θ_τ is, the more conservative the criterion becomes. As shown in Fig. 4(a) and (b), the red regions represent the

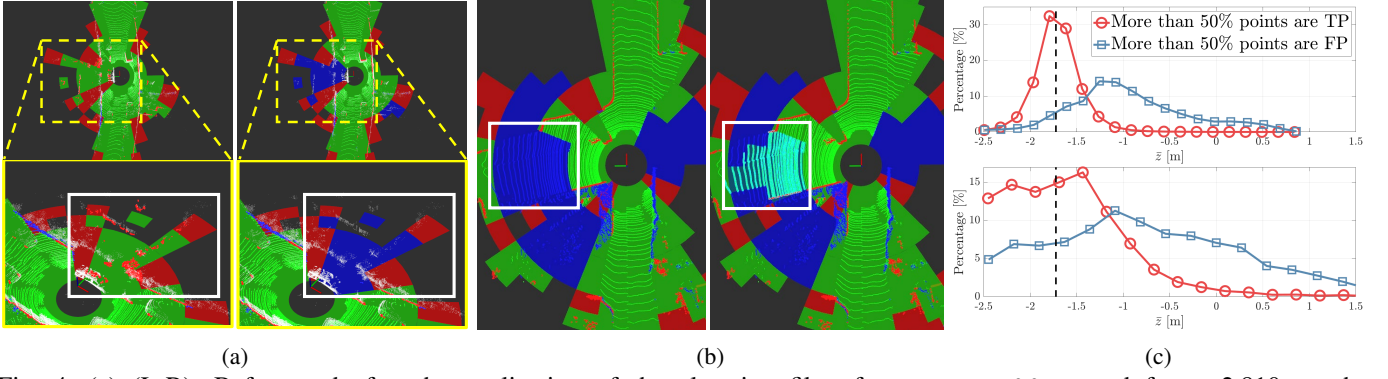


Fig. 4. (a) (L-R): Before and after the application of the elevation filter for sequence 00 around frame 2,810 on the SemanticKITTI dataset. Note that red cloud points which denote FPs are filtered. (b) (L-R): Before and after the application of flatness for sequence 10 around frame 286, where the cyan points denote reverted TPs via flatness, which are previously filtered through the elevation. The green, blue, and red regions denote regions where GLE is met, filtered by the elevation, and filtered by flatness, respectively. (c) (T-B): Probability Distribution Function (PDF) of the mean z value between two corresponding partial ground estimations \hat{G}_n by using uprightness alone in central zone Z_1 and quater zone Z_2 , and outer zone Z_4 on whole sequences of the SemanticKITTI dataset. The dashed line represents the ground elevation from a sensor (best viewed in color).

cases where the uprightness has not been met, so $\phi(\mathbf{v}_{3,n})$ is equal to zero. Through experiments, we set θ_τ to 45° , which is empirically determined to be strict enough (see Section IV.B). **Elevation** Unfortunately, it is not possible to filter the \hat{G}_n belonging to the bonnet or roof of a car by using uprightness alone. In addition, when large objects, such as cars, are close to the sensor frame, occlusion occurs, thus giving rise to the partial observation issue. That is, partially measured cloud points above the occluded spaces are predicted as the \hat{G}_n , which are not, in fact, the lowest parts in the space. This phenomenon is presented in the left in Fig. 4(a).

To tackle this problem, a conditional logistic function, or $\psi(\bar{z}_n, r_n)$, is proposed. The key idea of the elevation filter is motivated by Asvadi *et al.* [9]: once \bar{z}_n near the sensor frame is quite high compared with $-h_s$, \hat{G}_n is likely not the ground. The experimental evidence supports our rationale as shown in Fig. 4(c). Using uprightness alone, TPs and FPs become distinguishable based on \bar{z}_n with a minor loss of TPs when r_n is small, i.e. the case where \hat{G}_n is in Z_1 and Z_2 . In contrast, TPs and FPs are indistinguishable when r_n is large, i.e. the case where \hat{G}_n is in Z_4 .

Based on these observations, $\psi(\bar{z}_n, r_n)$ is defined as follows:

$$\psi(\bar{z}_n, r_n) = \begin{cases} (1 + e^{(\bar{z}_n - \kappa(r_n))})^{-1}, & \text{if } r_n < L_\tau \\ 1, & \text{otherwise} \end{cases} \quad (10)$$

where $\kappa(\cdot)$ denotes an adaptive midpoint function that exponentially increases depending on r_n . As visualized in Fig. 4(a), if \bar{z}_n is lower than $\kappa(r)$, then the value of $\psi(\bar{z}_n, r_n)$ is higher than 0.5 when r_n is smaller than constant range parameter L_τ . Note that $\psi(\bar{z}_n, r_n)$ always becomes 1 when r_n exceeds L_τ because it is unclear whether \hat{G}_n comes from non-ground objects or from a steep incline as r_n becomes larger.

Flatness Finally, the aim of flatness is to revert some FNs filtered by the elevation if they are definitely an even plane. For instance, if \hat{G}_n belongs to a very steep uphill, and thus if \bar{z}_n is larger than $\kappa(r)$, \hat{G}_n is sometimes filtered out via $\psi(\bar{z}_n, r_n)$. To resolve this problem, we leverage the surface



Fig. 5. (L-R) Our robot platform for additional experiments. Rough terrain environment on KAIST campus.

variable σ_n to check the flatness of \hat{G}_n which is considered to be FNs, even though $\psi(\bar{z}_n, r_n)$ is lower than 0.5. For this, one possible implementation of $\varphi(\psi(\bar{z}_n, r_n), \sigma_n)$ is defined as

$$\varphi(\psi(\bar{z}_n, r_n), \sigma_n) = \begin{cases} \zeta e^{-(\sigma_n - \sigma_{\tau,m})}, & \text{if } \psi(\bar{z}_n, r_n) < 0.5 \\ 1, & \text{otherwise} \end{cases} \quad (11)$$

where $\zeta > 1$ and $\sigma_{\tau,m}$ denote the magnitude of gain and the threshold of the surface variable depending on Z_m , respectively. By doing so, the GLE of steep uphill increases, and they can be reverted into the ground estimation although \bar{z}_n is higher than $\kappa(r_n)$.

Therefore, the final estimated ground points can be directly expressed as follows:

$$\hat{G} = \bigcup_{n \in \{N_C\}} [f(\mathcal{X}_n | \theta_n) > 0.5] \hat{G}_n \quad (12)$$

where $[\cdot]$ denotes the Iverson bracket, which returns **true** if the condition is satisfied and **false** otherwise.

IV. EXPERIMENTS

A. Dataset

SemanticKITTI Dataset To evaluate the ground segmentation performance of our proposed method against other ground segmentation algorithms, we experimented with the

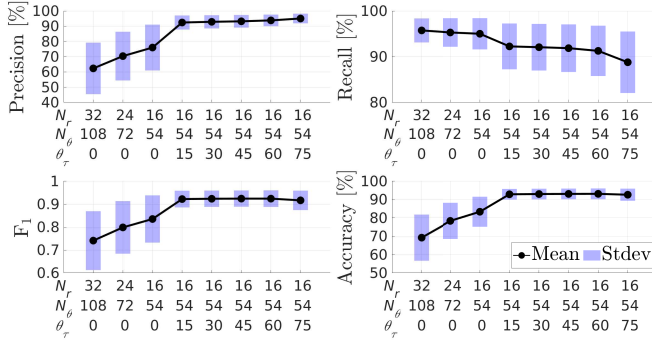


Fig. 6. Performance changes of uniform polar representation with varying bin sizes (N_r, N_θ) and uprightness threshold θ_τ on the SemanticKITTI dataset.

SemanticKITTI dataset [1]. Accordingly, the points annotated with selected classes, i.e. lane marking, road, parking, sidewalk, other ground, vegetation, and terrain, are considered to be ground-truth ground points to be extracted. Note that the vegetation contains leaves of trees, so only points whose z values with respect to the sensor frame are below -1.3 m are considered to be ground truths.

Rough Terrain Dataset Even though the SemanticKITTI dataset represents various urban environments, data were acquired from vehicle platforms on pavements only. Therefore, we conducted an additional, more challenging experiment to prove the robustness and generality of our proposed algorithm. As shown in Fig. 5, our robot platform is equipped with a 3D LiDAR (Ouster OS0-128). The data were acquired from a rough terrain environment on the KAIST campus, Daejeon, South Korea.

B. Error Metrics

To evaluate our proposed method quantitatively, *Precision*, *Recall*, *F₁ score*, and *Accuracy* are considered. Let N_{TP} , N_{TN} , N_{FP} , and N_{FN} be the number of points in TP, TN, FP, and FN, respectively; then, these metrics are defined as follows:

- Precision: $\frac{N_{TP}}{N_{TP} + N_{FP}}$, F_1 score: $\frac{2 \cdot N_{TP}}{2 \cdot N_{TP} + N_{FP} + N_{FN}}$
- Recall: $\frac{N_{TP}}{N_{TP} + N_{FN}}$, Accuracy: $\frac{N_{TP} + N_{TN}}{N_{TP} + N_{TN} + N_{FP} + N_{FN}}$

C. Parameters of Patchwork

We set $\{N_{r,1}, N_{r,2}, N_{r,3}, N_{r,4}\} = \{2, 4, 4, 4\}$, $\{N_{\theta,1}, N_{\theta,2}, N_{\theta,3}, N_{\theta,4}\} = \{16, 32, 54, 32\}$, $L_{\min} = 2.7$ m, and $L_{\max} = 80.0$ m for the CZM. For R-GPF, $N_{\text{seed}} = 20$, $z_{\text{seed}} = 0.5$, $M_d = 0.15$ and $M_h = -1.1$. The smaller z_{seed} and M_d are, the more conservative the criterion becomes. Finally, for GLE, $L_\tau = L_{\max,2}$, $\sigma_{\tau,1} = 0.00012$, and $\sigma_{\tau,2} = 0.0002$, for which cloud points whose σ_τ is lower than 0.01 are considered to be a plane [26], yet we set more strict criteria.

V. RESULTS AND DISCUSSION

A. Performance Analysis with Different Bin Sizes

First, the effect of bin size is analyzed, which was not conducted in our previous study [14]. As shown in Fig. 6,

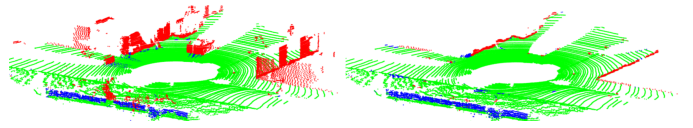


Fig. 7. (L) Ground estimation results from R-GPF [14] and (R) Patchwork for sequence 00 around frame 429 on the SemanticKITTI dataset. Our proposed GLE successfully rejects FPs, with green, blue, and red points denoting TPs, FNs, and FPs, respectively. The less red points are, the better it is (best viewed in color).

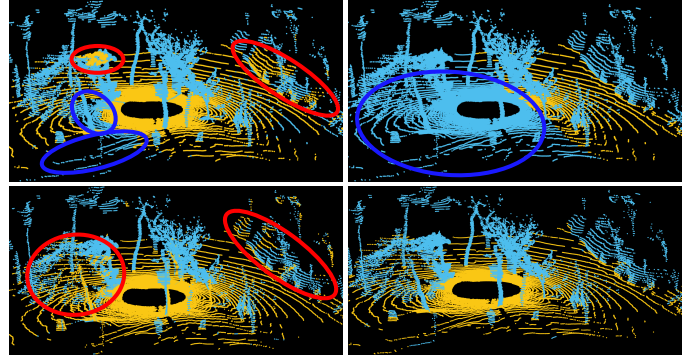


Fig. 8. Qualitative comparison of multiple plane fitting-based methods. (L-R, T-B): Output from GPF [8], CascadedSeg [12], R-GPF [14], and Patchwork on rough terrain. Our method shows its robustness even though the ground is bumpy and sloped. The yellow and cyan points denote estimated ground and non-ground, respectively. The points inside blue circles denote FNs and those inside red circles denote FPs (best viewed in color).

a larger bin size leads to a large improvement in precision with little recall degradation; thus, it raises the F_1 score dramatically. This result implies that the larger the bin area is, the more generally the ground can be estimated. However, it leads to lower recall as the bin size becomes larger due to the fact that the resolution of each bin is decreased.

B. Impact of Uprightness

Unfortunately, the naïve enlargement of bin size does not resolve the large variance of precision, as presented in Fig. 6. However, using only uprightness leads to a dramatic performance improvement in precision while reducing the variance and thus improves the F_1 score. Thus, the result shows that our uprightness successfully filters out the wrongly estimated partial ground. However, a higher θ_τ allows actual TPs, such as steep slope regions or boundary regions between roads and curbs, to be classified as non-ground, and thus recall is slightly decreased. Therefore, we can conclude that the θ_τ of 45° yielded the most reasonable estimation throughout the experiment.

C. Effectiveness of Ground Likelihood Estimation

Thereafter, the effectiveness of GLE is validated. As shown in Fig. 7, Fig. 8, and Table I, R-GPF, which is our baseline

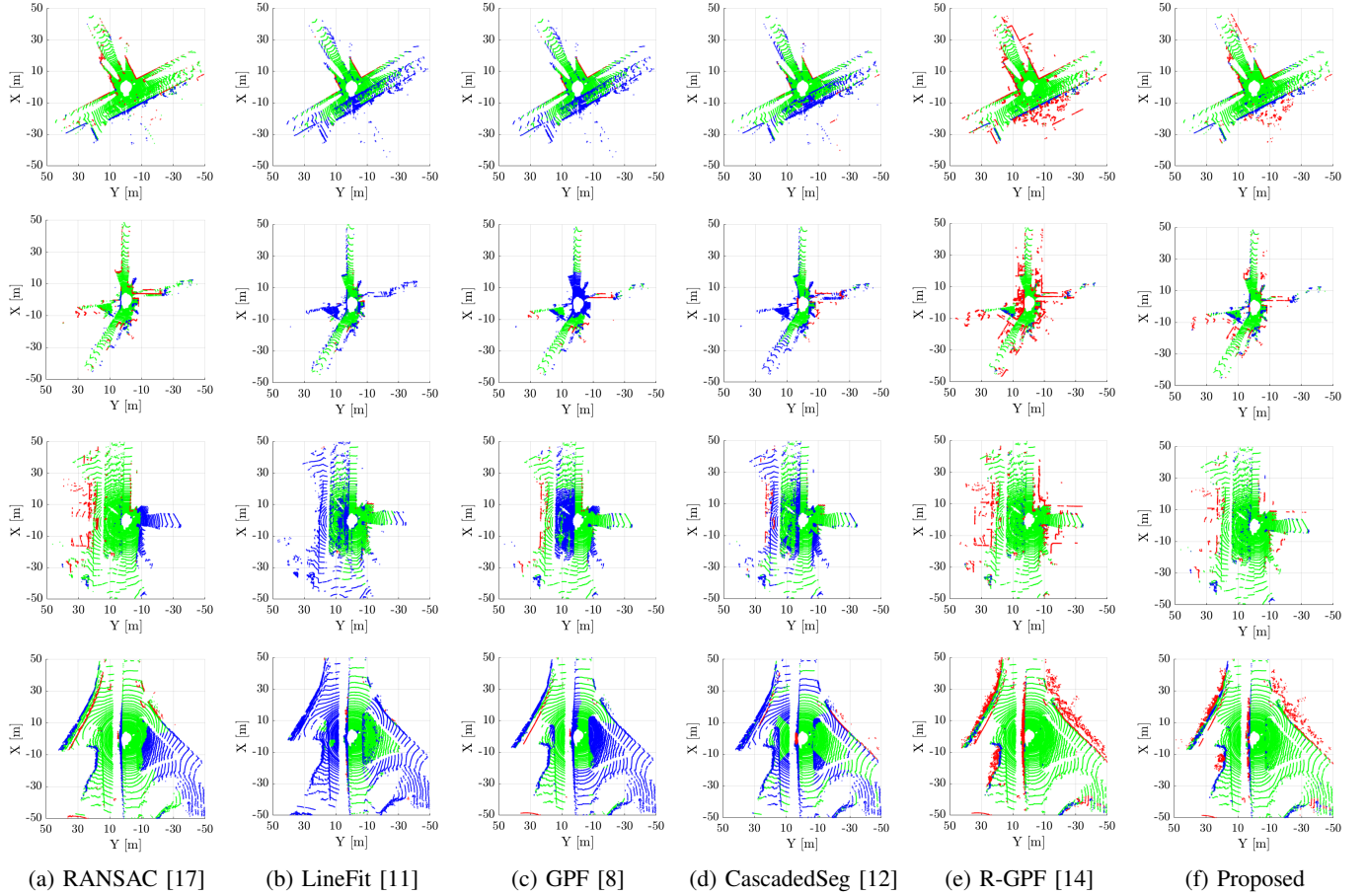


Fig. 9. Comparison of ground estimation results produced by the proposed method and state-of-the-art methods on the Semantic KITTI dataset (T-B): sequence 00 around frames 429 and 1,800, 06 around frame 505, and 01 around frame 180. The green, blue, and red points denote TPs, FNs, and FPs, respectively. For blue and red points, the less, the better and for green points, the more, the better (best viewed in color).

algorithm, estimates a ground plane with many FPs because R-GPF gives priority to the maximization of recall. Meanwhile, our GLE successfully filters out the wrongly estimated partial ground, thus dramatically reducing FNs. In particular, it is verified that many walls and a parked car can be rejected by the uprightness and elevation filters, respectively.

D. Comparison with State-of-the-Art Methods

Patchwork was quantitatively compared with state-of-the-art methods, namely, RANSAC [17], LineFit¹ [11], GPF² [8], and CascadedSeg³ [12]. We leveraged the open-source implementations for the experiment.

As shown in Fig. 9, other methods show detailed ground estimations. However, they struggle with non-planar regions, including a steep slope, a complex intersection, and a region where many curbs exist. In particular, LineFit is likely to be sensitive when encountering undulated terrains or bushy regions [12], estimating many FNs. On the other hand, some bins in GPF and CascadeSeg sometimes tend to converge to a local minimum because the bin size is too big, so it is not

TABLE I: Performance comparison with the state-of-the-art methods on whole sequences of the SemanticKITTI dataset. U, E, and F denote the uprightness, elevation, and flatness terms, respectively; the red color denotes low Precision/Recall and large standard deviations.

| Method | Precision [%] | | Recall [%] | | F ₁ |
|------------------|---------------|-------------|--------------|-------------|----------------|
| | μ | σ | μ | σ | |
| RANSAC [17] | 88.16 | 17.18 | 91.26 | 12.52 | 0.897 |
| GPF [8] | 95.84 | 3.41 | 79.57 | 21.08 | 0.870 |
| LineFit [11] | 98.17 | 1.47 | 78.26 | 9.29 | 0.871 |
| CascadedSeg [12] | 91.16 | 11.10 | 68.95 | 11.18 | 0.785 |
| R-GPF [14] | 66.94 | 16.50 | 93.34 | 3.41 | 0.780 |
| R-GPF [14] + U | 91.88 | 4.97 | 92.84 | 4.45 | 0.924 |
| CZM + U | 91.38 | 5.33 | 93.65 | 4.10 | 0.925 |
| CZM + U + E | 92.89 | 4.25 | 93.08 | 4.73 | 0.930 |
| CZM + U + E + F | 92.47 | 4.26 | 93.43 | 4.63 | 0.930 |

safe to assume that the ground is planar within the bin; in particular, this phenomenon becomes worse in rough terrain as presented in Fig. 8. Thus, they show the large variance of recall on the SemanticKITTI dataset as shown in Table I.

In contrast, our proposed method shows promising performance. In particular, our method estimates the ground with little variance of recall relative to other methods. This

¹https://github.com/lorenwel/linefit_ground_segmentation

²https://github.com/VincentCheungM/Run_based_segmentation

³https://github.com/n-patiphon/cascaded_ground_seg

TABLE II: Mean algorithm speed of multiple grid-based methods on sequence 05 of the SemanticKITTI dataset.

| Category | Baseline | Method | Runtime [Hz] |
|---------------|----------|------------------|--------------|
| Line fitting | - | LineFit [11] | 58.96 |
| | RANSAC | CascadedSeg [12] | 13.07 |
| Plane fitting | | GPF [8] | 29.72 |
| | PCA | R-GPF [14] | 35.30 |
| | | Patchwork (Ours) | 43.97 |

confirms that our method overcomes the under-segmentation problem and is thus robust against these corner cases in urban environments.

Meanwhile, one may observe from Fig. 9 that the number of FNs from Patchwork is larger than those of LinFit, GPF, and CascadedSeg, yet these are actually the lowest parts of some objects, as shown in Fig. 7. This means that even though FN degrades the performance of quantitative metrics, they rather help to resolve the under-segmentation issue.

E. Algorithm speed

To check the speed of each algorithm, we used Intel(R) Core(TM) i7-7700K CPU. Note that our proposed method shows the fastest speed among various multiple plane fitting-based methods as shown in Table II. In particular, it is surprising that Patchwork is faster than R-GPF. This is because our CZM reduces the number of bins, so the amount of plane fitting is also decreased; for instance, Patchwork uses 504 bins, whereas R-GPF uses 3,240 bins. Furthermore, our method is based on PCA, so it is also faster than CascadedSeg, which is a RANSAC-based method. Therefore, this result shows that our method is not only robust but also fast enough for preprocessing use.

VI. CONCLUSION

In this study, a fast and robust ground segmentation method, Patchwork, has been proposed. Our proposed method was proved to overcome the under-segmentation problem compared with previous approaches. In particular, our method provides a well-segmented ground estimation with smaller variations in performance, which enables mobile robots to detect non-ground objects in a robust way. In future works, we plan to apply our Patchwork to the detection of moving objects or to devise a deep learning-aided ground likelihood estimation for more sophisticated ground segmentation.

REFERENCES

- [1] J. Behley, M. Garbade, A. Milioto, J. Quenzel, S. Behnke, C. Stachniss, and J. Gall, "SemanticKITTI: A dataset for semantic scene understanding of LiDAR sequences," in *Proc. IEEE Int. Conf. Comput. Vis.*, 2019, pp. 9297–9307.
- [2] H. Lim, S. Hwang, S. Shin, and H. Myung, "Normal distributions transform is enough: Real-time 3D scan matching for pose correction of mobile robot under large odometry uncertainties," in *Proc. IEEE Int. Conf. Control, Automat. and Syst.*, 2020, pp. 1155–1161.
- [3] J. Byun, K. Na, B. Seo, and M. Roh, "Drivable road detection with 3D point clouds based on the MRF for intelligent vehicle," in *Proc. Field and Service Robotics*, 2015, pp. 49–60.
- [4] B. Douillard, J. Underwood, N. Kuntz, V. Vlaskine, A. Quadros, P. Morton, and A. Frenkel, "On the segmentation of 3D LiDAR point clouds," in *Proc. IEEE Int. Conf. Robot. Automat.*, 2011, pp. 2798–2805.

- [5] S. Thrun, M. Montemerlo, H. Dahlkamp, D. Stavens, A. Aron, J. Diebel, P. Fong, J. Gale, M. Halpenny, G. Hoffmann, *et al.*, "Stanley: The robot that won the DARPA Grand Challenge," *J. Field Robot.*, vol. 23, no. 9, pp. 661–692, 2006.
- [6] F. Moosmann, O. Pink, and C. Stiller, "Segmentation of 3D LiDAR data in non-flat urban environments using a local convexity criterion," in *Proc. IEEE Intell. Veh. Symp.*, 2009, pp. 215–220.
- [7] A. Milioto, I. Vizzo, J. Behley, and C. Stachniss, "RangeNet++: Fast and accurate LiDAR semantic segmentation," in *Proc. IEEE/RSJ Int. Conf. Intell. Robots Syst.*, 2019, pp. 4213–4220.
- [8] D. Zermas, I. Izzat, and N. Papanikolopoulos, "Fast segmentation of 3D point clouds: A paradigm on LiDAR data for autonomous vehicle applications," in *Proc. IEEE Int. Conf. Robot. Automat.*, 2017, pp. 5067–5073.
- [9] A. Asvadi, P. Peixoto, and U. Nunes, "Detection and tracking of moving objects using 2.5D motion grids," in *Proc. IEEE Int. Conf. Intell. Transport. Syst.*, 2015, pp. 788–793.
- [10] W. Ali, S. Abdelkarim, M. Zidan, M. Zahran, and A. El Sallab, "Yolo3D: End-to-end real-time 3D oriented object bounding box detection from LiDAR point cloud," in *Proc. European Conf. Comput. Vis. Workshops*, 2018.
- [11] M. Himmelsbach, F. V. Hundelshausen, and H.-J. Wuensche, "Fast segmentation of 3D point clouds for ground vehicles," in *Proc. IEEE Intell. Veh. Symp.*, 2010, pp. 560–565.
- [12] P. Narksri, E. Takeuchi, Y. Ninomiya, Y. Morales, N. Akai, and N. Kawaguchi, "A slope-robust cascaded ground segmentation in 3D point cloud for autonomous vehicles," in *Proc. IEEE Int. Conf. Intell. Transport. Syst.*, 2018, pp. 497–504.
- [13] K. Na, B. Park, and B. Seo, "Drivable space expansion from the ground base for complex structured roads," in *Proc. IEEE Int. Conf. on Systems, Man, and Cybernetics*, 2016, pp. 373–378.
- [14] H. Lim, S. Hwang, and H. Myung, "ERASOR: Egocentric ratio of pseudo occupancy-based dynamic object removal for static 3D point cloud map building," *IEEE Robot. Automat. Lett.*, vol. 6, no. 2, pp. 2272–2279, 2021.
- [15] A. Asvadi, C. Premevida, P. Peixoto, and U. Nunes, "3D LiDAR-based static and moving obstacle detection in driving environments: An approach based on voxels and multi-region ground planes," *Robot. Auton. Syst.*, vol. 83, pp. 299–311, 2016.
- [16] J. Cheng, D. He, and C. Lee, "A simple ground segmentation method for LiDAR 3D point clouds," in *Proc. IEEE Int. Conf. on Advances in Comput. Tech., Info. Science and Commun.*, 2020, pp. 171–175.
- [17] M. A. Fischler and R. C. Bolles, "Random sample consensus: A paradigm for model fitting with applications to image analysis and automated cartography," *Commun. ACM*, vol. 24, no. 6, pp. 381–395, 1981.
- [18] T. Chen, B. Dai, R. Wang, and D. Liu, "Gaussian-process-based real-time ground segmentation for autonomous land vehicles," *J. Intell. Robot. Syst.*, vol. 76, no. 3–4, pp. 563–582, 2014.
- [19] R. Tse, N. Ahmed, and M. Campbell, "Unified mixture-model based terrain estimation with Markov Random Fields," in *Proc. IEEE Int. Conf. on Multisensor Fusion and Integration for Intell. Syst.*, 2012, pp. 238–243.
- [20] L. Rummelhard, A. Paigwar, A. Nègre, and C. Laugier, "Ground estimation and point cloud segmentation using spatiotemporal conditional random field," in *Proc. IEEE Intell. Veh. Symp.*, 2017, pp. 1105–1110.
- [21] D. Steinhäuser, O. Ruepp, and D. Burschka, "Motion segmentation and scene classification from 3D LiDAR data," in *Proc. IEEE Intell. Veh. Symp.*, 2008, pp. 398–403.
- [22] A. Paigwar, Ö. Erkent, D. S. González, and C. Laugier, "GndNet: Fast ground plane estimation and point cloud segmentation for autonomous vehicles," in *Proc. IEEE/RSJ Int. Conf. Intell. Robots Syst.*, 2020.
- [23] K. Wong, S. Wang, M. Ren, M. Liang, and R. Urtasun, "Identifying unknown instances for autonomous driving," in *Proc. PMLR Conf. on Robot Learning*, 2020, pp. 384–393.
- [24] A. Nurunnabi, D. Belton, and G. West, "Diagnostics based principal component analysis for robust plane fitting in laser data," in *Proc. IEEE Int'l Conf. Comput. Info. Tech.*, 2014, pp. 484–489.
- [25] H. Lim, C. Park, and H. Myung, "RONet: Real-time range-only indoor localization via stacked bidirectional LSTM with residual attention," in *Proc. IEEE/RSJ Int. Conf. Intell. Robots Syst.*, 2019, pp. 3241–3247.
- [26] B. Eckart, K. Kim, and J. Kautz, "HGMR: Hierarchical gaussian mixtures for adaptive 3D registration," in *Proc. European Conf. Comput. Vis.*, 2018, pp. 705–721.